

model, it is possible to change one element ( $R_{gs}$ ) and then to compensate others to reestablish a good fit. However, the fact that an improved fit is achieved when the first slice is allowed to differ suggests that there are significant differences in the field structure in the gate feed region. In particular, the source resistance is large in the first slice and negligible in the remainder. This could be associated with the perturbation of the channel near the source by the gate feed. A model based more directly on the underlying physics of the device would be necessary in order to quantify these differences accurately.

#### CONCLUSION

It has been shown that an improvement in fitting of a HEMT device model to measured signal and noise parameters can be brought about by using a sliced model to account for the effects of the distributed nature of the gate and drain electrodes, and by allowing the first slice to differ from the others in order to account for the difference in field structure in the gate feed region.

#### ACKNOWLEDGMENT

We wish to thank the UK Science and Engineering Research Council for a research studentship for M. T. Hickson.

#### REFERENCES

- [1] R. A. Pucel, H. A. Haus, and H. Statz, "Signal and noise properties of GaAs microwave FET," in *Advances in Electronics and Electron Physics*, vol. 38, L. Morton, Ed. New York: Academic Press, 1975.
- [2] T. M. Brookes, "The noise properties of high electron mobility transistors," *IEEE Trans. Electron Devices*, vol. ED-33, pp. 52-57, Jan. 1986.
- [3] A. Cappy, A. Vanoverschelde, M. Schortgen, C. Versnaeyen, and G. Salmer, "Noise modelling in submicrometer-gate two-dimensional electron gas field effect transistors," *IEEE Trans. Electron Devices*, vol. ED-32, pp. 2787-2795, Dec. 1985.
- [4] C. Moglestue, "A Monte Carlo particle study of the intrinsic noise figure in GaAs MESFET," *IEEE Trans. Electron Devices*, vol. ED-32, pp. 2092-2096, Oct. 1985.
- [5] H. Fukui, "Design of Microwave GaAs MESFETs for broadband, low-noise amplifiers," *IEEE Trans. Microwave Theory Tech.*, vol. MTT-27, pp. 643-650, July 1979.
- [6] H. Fukui, "Optimal noise figure of microwave GaAs MESFETs," *IEEE Trans. Electron Devices*, vol. ED-26, pp. 1032-1037, July 1979.
- [7] A. F. Podell, "A functional GaAs FET noise model," *IEEE Trans. Electron Devices*, vol. ED-28, pp. 511-517, May 1981.
- [8] M. S. Gupta and P. T. Greiling, "Microwave noise characterization of GaAs MESFETs: Determination of extrinsic noise parameters," *IEEE Trans. Microwave Theory Tech.*, vol. 36, pp. 745-751, Apr. 1988.
- [9] M. W. Pospieszalski, "Modeling of noise parameters of MESFETs and MODFETs and their frequency and temperature dependence," *IEEE Trans. Microwave Theory Tech.*, vol. 37, pp. 1340-1350, Sept. 1989.
- [10] W. Heinrich, "Limits of FET modelling by lumped elements," *Electron. Lett.*, vol. 22, pp. 630-632, June 1986.
- [11] L. Escotte and J. Mollier, "Semidistributed model of millimeter-wave FET for S-parameter and noise figure predictions," *IEEE Trans. Microwave Theory Tech.*, vol. 38, pp. 748-753, June 1990.
- [12] C. H. Oxley and A. J. Holden, "Simple models for high-frequency MESFETs and comparison with experimental results," *Proc. Inst. Elec. Eng.*, vol. 133, pt. H, pp. 335-340, Oct. 1986.
- [13] *Touchstone and Libra User's Guide*, EEsof Inc., USA, July 1989.
- [14] A. D. Patterson, V. F. Fusco, J. J. McKeown, and J. A. C. Stewart, "Problems associated with small signal MESFET equivalent circuit model parameter extraction," in *Dig. 14th ARMMS Conf.*, Queens University, Belfast, Mar. 1991.

## Accurate Modeling of Axisymmetric Two-Port Junctions in Coaxial Lines Using the Finite Element Method

Waymond R. Scott, Jr.

**Abstract**—A technique is developed for analyzing axisymmetric two-port junctions (axisymmetric discontinuities) in coaxial lines using the finite element method. Boundary conditions are developed for the input and output ports that absorb the reflected and transmitted waves while injecting the incident wave. The use of higher order elements is shown to greatly improve the accuracy, i.e., the accuracy increases rapidly with the order of the elements even when the number of nodes is kept roughly constant. The accuracy of the technique is verified by comparison with the theoretical and experimental results of other investigators for three discontinuities, and the agreement is shown to be excellent.

#### INTRODUCTION

Discontinuities in coaxial lines are part of many microwave devices. Accurate models of these discontinuities are needed in the design of the devices. Traditionally the discontinuities have been modeled using mode matching and variational techniques; however, these techniques require a significant amount of analytical analysis for each geometry and become very complex for all but relatively simple geometries.

In this work, the finite element method (FEM) will be used to accurately model axisymmetric two-port junctions (axisymmetric discontinuities) in coaxial lines. The flexibility of the FEM allows more complicated geometries to be modeled. The addition of materials into the junction and complex geometrical shapes do not add any complications to the analysis. Furthermore, very accurate results are obtainable with the FEM with reasonable computational efficiency when higher order elements are used. To demonstrate the flexibility and the accuracy obtainable with the FEM, three discontinuities are analyzed, and the results are compared to theoretical and experimental results of other investigators. The agreement is shown to be excellent; even though in each of these discontinuities, the fields are singular at a corner on the center conductor and no special analysis is performed in this work to take the singularities into account. For one of the cases, the accuracy versus the order of the elements from first to fourth order is investigated.

This work compliments the work of other investigators who have used the FEM to investigate axisymmetric problems: Marouby *et al.* [1] and Wilkins *et al.* [2] have investigated transitions between coaxial lines; and Silvester and Konrad [3], [4] and Daly [5] have investigated the modes in axisymmetric resonators.

#### FORMULATION

Fig. 1 is a schematic diagram of a general coaxial discontinuity in which the region to be modeled with the FEM is indicated. For this analysis, the incident wave is assumed to be a TEM mode. The

Manuscript received September 10, 1991; revised January 14, 1992. This work was supported in part by the Georgia Tech Material Metrology Consortium, the Georgia Tech Manufacturing Research Center, and the Joint Services Electronics Program under Contracts DAAL 03-87-K-0059 and DAAL-03-90-C-0004.

The author is with the Georgia Institute of Technology, School of Electrical Engineering, Atlanta, GA 30332.

IEEE Log Number 9200860.

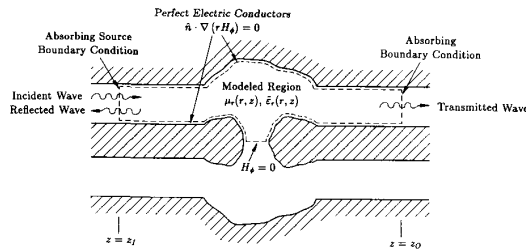


Fig. 1. General axisymmetric coaxial discontinuity.

discontinuity will reflect and transmit a portion of the incident wave and will also generate higher order modes; however, the frequency range is restricted so that the higher order modes are cut off in the coaxial lines. The higher order modes may or may not be cut off in the discontinuity. The lengths of the input and output coaxial lines are chosen to be sufficiently long so that the fields at the input and output ports are essentially TEM. In this work, the electromagnetic fields are calculated in the indicated region for a given incident wave. The reflection and transmission coefficients of the discontinuity are then computed from the fields at the input and output ports.

Only TM modes will exist in the device, when the geometry and the material properties are restricted to be axisymmetric and the excitation is restricted to be TM:  $\vec{H} = H_\phi(r, z)\hat{\phi}$  and  $\vec{E} = E_r(r, z)\hat{r} + E_z(r, z)\hat{z}$ . The fields are governed by the vector Helmholtz equations, and since only one component of  $\vec{H}$  exists, the vector Helmholtz equation for  $\vec{H}$  can be reduced to a single scalar equation in  $H_\phi$ :

$$\nabla \times \left( \frac{1}{\bar{\epsilon}} \nabla \times \vec{H} \right) - \omega^2 \mu \vec{H} = 0 \quad (1)$$

becomes

$$\nabla \cdot \left( \frac{1}{\bar{\epsilon}_r} \nabla H_\phi \right) - \frac{1}{\bar{\epsilon}_r r^2} H_\phi + \mu_r k_o^2 H_\phi + \frac{1}{r} \frac{\partial}{\partial r} \left( \frac{1}{\bar{\epsilon}_r} \right) H_\phi = 0 \quad (2)$$

where  $\bar{\epsilon} = \bar{\epsilon}_r \epsilon_o = \epsilon - j\sigma/\omega$  is the complex effective permittivity,  $\mu = \mu_r \mu_o = \mu' - j\mu''$  is the complex permeability,  $k_o = \omega \sqrt{\mu_o \epsilon_o}$  is the wavenumber, and an  $e^{j\omega t}$  time dependence is assumed. The two components of  $\vec{E}$  can be obtained from  $H_\phi$  using one of Maxwell's curl equations.

A solution to (2) subject to the appropriate boundary conditions is determined using the FEM. Galerkin's method is used in the formulation [6]. The region of interest is divided up into elements. The elements are generated by rotating planar triangular elements about the z-axis to sweep out an annular volume. Let  $V^{(e)}$  be the volume swept out by element (e),  $S^{(e)}$  be the surface of the volume,  $A^{(e)}$  be the cross-sectional area of the planar element, and  $\Gamma^{(e)}$  be the boundary of the planar element. In Galerkin's method residual integrals are computed for each of the weighting functions  $W_i$ . The contribution of element (e) to the residual integral for the weighting function  $W_i$  is

$$R_i^{(e)} = - \int_{V^{(e)}} W_i \left[ \nabla \cdot \left( \frac{1}{\bar{\epsilon}_r} \nabla H_\phi \right) - \frac{1}{\bar{\epsilon}_r r^2} H_\phi + \mu_r k_o^2 H_\phi + \frac{1}{r} \frac{\partial}{\partial r} \left( \frac{1}{\bar{\epsilon}_r} \right) H_\phi \right] dV. \quad (3)$$

This equation is rearranged to obtain a boundary integral in a form that allows the boundary conditions to be enforced in a straight-

forward manner:

$$R_i^{(e)} = - \oint_{S^{(e)}} W_i \frac{1}{\bar{\epsilon}_r r} \nabla(rH_\phi) \cdot d\vec{S} + \int_{V^{(e)}} \left\{ \frac{1}{\bar{\epsilon}_r} \nabla W_i \cdot \nabla H_\phi + \frac{1}{\bar{\epsilon}_r r} \hat{r} \cdot \nabla(W_i H_\phi) + W_i \left[ \frac{1}{\bar{\epsilon}_r r^2} H_\phi - \mu_r k_o^2 H_\phi \right] \right\} dV. \quad (4)$$

The weighting functions are chosen to be  $W_i = \sqrt{r} \alpha_i(r, z)$ , and  $H_\phi$  is expanded in terms of the basis functions  $H_\phi = \sum_j H_j \sqrt{r} \alpha_j(r, z)$ , where the  $\alpha$ 's are the usual finite element basis functions. The  $\sqrt{r}$  term is included to eliminate the  $1/r$  terms in (4); this makes it possible to evaluate and store the resulting integrals in universal matrices. The basis functions are the interpolation polynomials for the elements. Triangular elements of first order have three linear basis functions, and triangular elements of order  $n$  have  $(n + 1)(n + 2)/2$  polynomial basis functions of order  $n$ , one for each node of the elements [7].

Using the above weighting and basis functions and evaluating the  $\phi$  integral, (4) becomes

$$R_i^{(e)} = -2\pi \oint_{\Gamma^{(e)}} W_i \frac{1}{\bar{\epsilon}_r} \nabla(rH_\phi) \cdot d\vec{\Gamma} + 2\pi \sum_j H_j \int_{A^{(e)}} \left\{ \frac{r^2}{\bar{\epsilon}_r} \nabla \alpha_i \cdot \nabla \alpha_j + \frac{3r}{2\bar{\epsilon}_r} \hat{r} \cdot \nabla(\alpha_i \alpha_j) + \left[ \frac{9}{4\bar{\epsilon}_r} - \mu_r k_o^2 r^2 \right] \alpha_i \alpha_j \right\} dA \quad (5)$$

where  $d\vec{\Gamma} = \hat{n} d\Gamma$  is normal to the boundary. Here  $\bar{\epsilon}_r$  and  $\mu_r$  are restricted to be constant in each element to simplify the evaluation of the integrals. The area integrals are evaluated and stored in universal matrices using techniques similar to those of Silvester [8].

For the portion of the boundary between two adjacent elements, the boundary integrals will sum to zero when  $\hat{n} \cdot \nabla(rH_\phi)/\bar{\epsilon}_r$  is continuous across the boundary. When the total residual equations are assembled, these integrals are replaced by their desired value, zero. This will tend to force  $\hat{n} \cdot \nabla(rH_\phi)/\bar{\epsilon}_r$  to be continuous across the boundary between the elements, which is equivalent to the tangential component of  $\vec{E}$  being continuous across the boundary. The boundary integral also gives the correct "natural boundary condition" for a perfect electric conductor,  $\hat{n} \cdot \nabla(rH_\phi) = 0$ . The boundary condition for the tangential component of  $\vec{H}$  ( $H_\phi$ ) and the normal component of  $\vec{E}$  are met by forcing  $H_\phi$  to be continuous across the boundary. The boundary condition for a perfect magnetic conductor and for boundaries with  $r = 0$  is  $H_\phi = 0$ .

At the input port, a boundary condition that will inject the incident wave and absorb the reflected wave is needed, and at the output port a boundary condition that will absorb the transmitted wave is needed. These boundary conditions are derived assuming that only the TEM mode exists at the input and output ports. The boundary conditions are derived from the differentiated transmission line equations; for the input port,

$$\left. \frac{dH_\phi}{dz} \right|_{z=z_i} = -jk(2H_i - H_\phi) \quad (6)$$

where  $H_i$  is the value of the incident field at the input port, and for the output port,

$$\left. \frac{dH_\phi}{dz} \right|_{z=z_o} = -jkH_\phi \quad (7)$$

where the wavenumber  $k = \omega \sqrt{\mu\epsilon}$ . These boundary conditions are applied by substituting them into the boundary integrals. The boundary integrals are evaluated and stored in universal matrices in a manner similar to that used for the area integrals.

## RESULTS

Three coaxial discontinuities are investigated to demonstrate the technique: A coaxial line with a stepped center conductor, a shielded open-circuited coaxial line, and a dielectrically loaded shielded open-circuited line. These discontinuities were chosen because they have been accurately characterized by other investigators, and, therefore, will provide a good test of the accuracy of the present technique.

### STEPPED COAXIAL LINE

Fig. 2(a) is a sketch of a stepped coaxial line. The FEM is used to calculate the reflection coefficient  $\rho$  and transmission coefficient  $\tau$  of the step. The effect of the higher order modes excited near the step can be modeled by a shunt, frequency dependent capacitor at the step. The capacitance is calculated from the reflection coefficient. The modeled region is divided up into 256 fourth order triangular elements with a total of 2156 nodes. The size of the elements is graded with the smallest elements adjacent to the edge at which  $\nabla H_\phi$  is singular. The size of the elements increases as the distance from the edge increases. A simple easily generated arrangement of elements was used. A more efficient arrangement of the elements would yield comparable accuracy with fewer elements.

The capacitance is tabulated and compared to that calculated by a mode matching method (MMM) [9] in Table I for frequencies from 1 GHz to 18 GHz. The relative differences between the capacitances and the reflection and transmission coefficients calculated using the FEM and the MMM are also tabulated in Table I:  $D_A = 2 |(\Delta_{FEM} - \Delta_{MMM}) / (\Delta_{FEM} + \Delta_{MMM})|$  where  $\Delta = C, \rho,$  and  $\tau$ . The agreement is seen to be excellent, with the relative differences between the capacitances varying between  $8.4 \times 10^{-5}$  and  $1.2 \times 10^{-3}$ . The largest differences are at the lower frequencies, where the reflection coefficient is not very sensitive to the value of the capacitance; this causes a small difference in the reflection coefficient to become a larger difference in the capacitance. The relative differences for the reflection and transmission coefficients vary between  $8.5 \times 10^{-6}$  and  $1.5 \times 10^{-4}$ , with the largest differences at the higher frequencies.

The capacitance values and the relative differences at 1 GHz are tabulated in Table II for five cases. In the first four cases, the total number of nodes for each case is approximately 2000, and the order of the elements varies from first to fourth. The relative differences are seen to decrease rapidly with increasing order: the first order results are seen to be very poor, while the fourth order results are seen to be excellent. In the last case, even though only 365 nodes and 40 fourth order elements are used, the relative differences are seen to be much smaller than those for the cases which use first and second order elements even though more than five times as many nodes are used for these cases.

### SHIELDED OPEN-CIRCUITED COAXIAL LINE

Fig. 2(b) is a sketch of a shielded open-circuited coaxial line. The shielded open circuit is commonly used as a calibration standard for network analyzers; it can be modeled by a perfect open circuit offset a small distance beyond the end of the center conductor. The boundary condition for a perfect electric conductor is

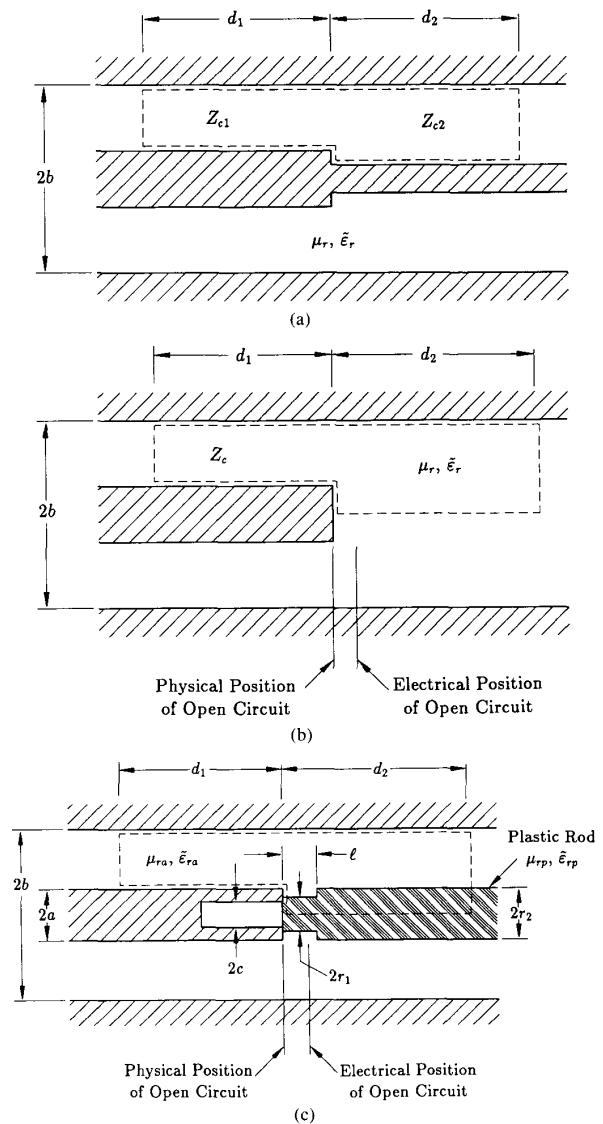


Fig. 2. (a) Stepped coaxial line. (b) Shielded open-circuited coaxial line. (c) Dielectrically loaded shielded open-circuited coaxial line.

TABLE I  
STEP CAPACITANCES AND RELATIVE DIFFERENCES  $D_C$ ,  $D_\rho$ , AND  $D_\tau$  AS A  
FUNCTION OF FREQUENCY WITH  $2b = 7$  mm,  $d_1 = d_2 = 2b$ ,  
 $Z_{c1} = 50 \Omega$ ,  $Z_{c2} = 75 \Omega$ ,  $\mu_r = 1$ , AND  $\epsilon_r = 1$

Freq. (GHz)	$C_{FEM}$ (fF)	$C_{MMM}$ (fF)	Relative Differences		
			$D_C$	$D_\rho$	$D_\tau$
1	10.005	9.992	$1.2 \times 10^{-3}$	$2.2 \times 10^{-5}$	$1.1 \times 10^{-5}$
2	9.986	9.995	$8.9 \times 10^{-4}$	$2.4 \times 10^{-5}$	$8.5 \times 10^{-6}$
4	9.993	10.005	$1.2 \times 10^{-3}$	$5.5 \times 10^{-5}$	$9.6 \times 10^{-6}$
6	10.011	10.022	$1.1 \times 10^{-3}$	$7.4 \times 10^{-5}$	$1.2 \times 10^{-5}$
8	10.036	10.045	$9.2 \times 10^{-4}$	$8.5 \times 10^{-5}$	$1.5 \times 10^{-5}$
10	10.067	10.076	$8.8 \times 10^{-4}$	$1.0 \times 10^{-4}$	$1.8 \times 10^{-5}$
12	10.106	10.115	$8.9 \times 10^{-4}$	$1.2 \times 10^{-4}$	$2.2 \times 10^{-5}$
14	10.152	10.161	$8.2 \times 10^{-4}$	$1.4 \times 10^{-4}$	$2.8 \times 10^{-5}$
16	10.209	10.215	$5.6 \times 10^{-4}$	$1.4 \times 10^{-4}$	$3.5 \times 10^{-5}$
18	10.277	10.278	$8.4 \times 10^{-5}$	$1.1 \times 10^{-4}$	$4.5 \times 10^{-5}$

TABLE II  
STEP CAPACITANCES AND RELATIVE DIFFERENCES  $D_c$ ,  $D_\rho$ , AND  $D_r$  AT 1 GHz AS A FUNCTION OF ELEMENT ORDER AND NUMBER OF NODES WITH  $2b = 7$  mm,  $d_1 = d_2 = 2b$ ,  $Z_{c1} = 50 \Omega$ ,  $Z_{c2} = 75 \Omega$ ,  $\mu_r = 1$ , AND  $\epsilon_r = 1$

Order	Number of Nodes	Number of Elem.	$C_{FEM}$ (fF)	Relative Differences		
				$D_c$	$D_\rho$	$D_r$
1	2055	3906	871.60	2.0	$9.4 \times 10^{-1}$	$3.7 \times 10^{-1}$
2	2021	960	28.143	$9.5 \times 10^{-1}$	$2.1 \times 10^{-2}$	$5.4 \times 10^{-3}$
3	1990	420	10.518	$5.1 \times 10^{-2}$	$6.0 \times 10^{-4}$	$1.6 \times 10^{-4}$
4	2156	256	10.005	$1.2 \times 10^{-3}$	$2.2 \times 10^{-5}$	$1.1 \times 10^{-5}$
4	365	40	10.823	$8.0 \times 10^{-2}$	$9.7 \times 10^{-4}$	$3.4 \times 10^{-4}$

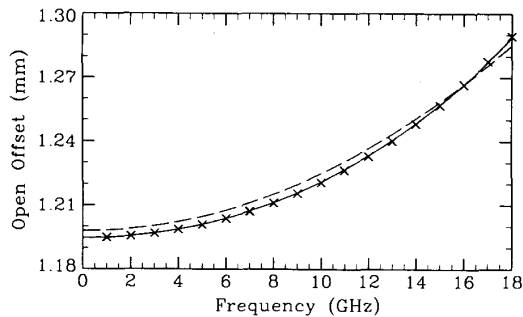


Fig. 3. Graph of the open offset for the shielded open-circuited coaxial line as a function of frequency with  $2b = 7$  mm,  $d_1 = 2b$ ,  $d_2 = 3b$ ,  $Z_c = 50 \Omega$ ,  $\mu_r = 1$ , and  $\epsilon_r = 1$ :  $\times \times \times$  finite element results, — variational results, and - - - experimental results.

placed on the right most boundary. This boundary is sufficiently far from the end of the center conductor so that it has an insignificant effect on the position of the open. The region is divided up into 288 fourth order triangular elements with a total of 2417 nodes. The size of the elements is graded with the smallest elements adjacent to the  $90^\circ$  corner at the end of the center conductor. The size of the elements increases as the distance from the edge increases. The offset of the open is calculated from the reflection coefficient calculated with the FEM. Fig. 3 is a graph of the open offset as a function of frequency from this work, from a formula fit to results calculated from a variational method [10], and from a formula fit to experimental results [11]. The agreement is seen to be excellent. The finite element and the variational results are seen to be almost identical, while the experimental results are seen to differ slightly. The difference in the position is  $3.4 \times 10^{-3}$  mm at 1 GHz and  $4.3 \times 10^{-3}$  mm at 18 GHz, which corresponds to a difference in the phase of the reflection coefficient of only  $8.2 \times 10^{-3}$  degrees at 1 GHz and  $1.9 \times 10^{-1}$  degrees at 18 GHz; these differences can be easily attributed to experimental errors.

#### DIELECTRICALLY LOADED SHIELDED OPEN-CIRCUITED COAXIAL LINE

Fig. 2(c) is a sketch of a dielectrically loaded shielded open-circuited coaxial line. This open closely approximates the Hewlett Packard 7 mm open circuit termination (part number 1250-1873) used to calibrate the Hewlett Packard 8510 network analyzer [12]. The plastic rod is used to depress the collet of a APC-7 coaxial connector. The relative permittivity of the plastic rod is  $\epsilon_{rp} = 2.56$  [13]. The hole in the collet is modeled; however, the fine details of the collet are not included. The region modeled is indicated in Fig. 2(c); note that the hole is not included in the region. All of

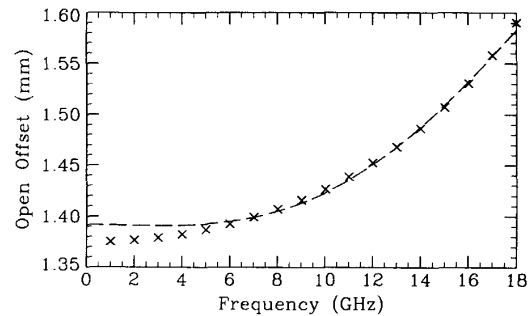


Fig. 4. Graph of the open offset for the dielectrically loaded shielded open-circuited coaxial line as a function of frequency with  $2a = 1.98$  mm,  $2b = 7$  mm,  $2c = 1.44$  mm,  $2r_1 = 1.98$  mm,  $2r_2 = 3.04$  mm,  $l = 1.98$  mm,  $d_1 = 2b$ ,  $d_2 = 3b$ ,  $\mu_{ro} = 1$ ,  $\epsilon_{ro} = 1$ ,  $\mu_{rp} = 1$ , and  $\epsilon_{rp} = 2.56$ :  $\times \times \times$  finite element results and - - - experimental results.

the modes that can propagate in the hole are strongly cutoff at the frequencies considered; thus, the portion of the boundary adjacent to the hole can be modeled by a perfect magnetic conductor. The region is divided up into 312 fourth order triangular elements with a total of 2613 nodes. The size of the elements is graded in the same manner as for the previous example. The offset of the open is calculated from the reflection coefficient calculated with the FEM. Fig. 4 is a graph of the open offset as a function of frequency from this work and from a formula fit to experimental results [12]. This formula is the one used to characterize the open when it is used in the calibration of the HP8510 network analyzer. The agreement is excellent; however, the results are seen to differ slightly. The differences at the lower frequencies are probably due to experimental errors in the measurement of the phase of the reflection coefficient, because the offset is very sensitive to phase errors at the lower frequencies. For example, the difference in the offset at 1 GHz is  $1.6 \times 10^{-2}$  mm which corresponds to a difference in the phase of the reflection coefficient of only  $3.8 \times 10^{-2}$  degrees.

#### CONCLUSIONS

A technique for modeling axisymmetric two-port junctions in coaxial lines was developed. The technique was verified and shown to be very accurate for three different geometries. The accuracy of the results was shown to increase rapidly when the order of the elements was increased. The accurate results were obtained with reasonable computational efficiency even though no special analysis was performed to take into account the singularities in the fields at the corners of the center conductors. The same accuracy could be obtained with fewer elements if the singularities were taken into account; however, this would complicate the analysis. A geometry that does not have a singularity in the fields is easier to model; thus, the same accuracy could be obtained with fewer elements. The geometries studied in this work are relatively simple; however, more complicated geometries can be modeled without any additional analysis, only the gridding up of the elements becomes more complicated.

#### REFERENCES

- [1] E. Marouby, M. Aubourg, and P. Guillon, "Application of the finite element method to the design of transitions between coaxial lines," *Proc. Inst. Elec. Eng.*, vol. 137, pt. H, no. 4, Aug. 1990.
- [2] G. M. Wilkins, Jin-Fa Lee, and R. Mittra, "Numerical modeling of axisymmetric coaxial waveguide discontinuities," *IEEE Trans. Microwave Theory Tech.*, vol. 39, no. 8, Aug. 1991.
- [3] P. Silvester and A. Konrad, "Axisymmetric triangular finite elements

- for the scalar helmholtz equation," *Int. J. Numer. Meth. Eng.*, vol. 5, pp. 481-497, 1973.
- [4] A. Konrad and P. Silvester, "Triangular finite elements for the generalized bessel equation of order  $m$ ," *Int. J. Numer. Meth. Eng.*, vol. 7, pp. 43-55, 1973.
- [5] P. Daly, "An alternative high-order finite element formulation for cylindrical field problems," *Int. J. Numer. Meth. Eng.*, vol. 19, pp. 1063-1072, 1983.
- [6] D. S. Burnett, *Finite Element Analysis from Concepts to Applications*. Reading, MA: Addison-Wesley, 1987.
- [7] P. P. Silvester and R. L. Ferrari, *Finite Elements for Electrical Engineers*, 2nd Ed. Cambridge University Press, Cambridge, 1990.
- [8] P. Silvester, "Construction of triangular finite element universal matrices," *Int. J. Numer. Meth. Eng.*, vol. 12, pp. 237-244, 1978.
- [9] A. Jurkus, "Computation of step discontinuities in coaxial line," *IEEE Trans. Microwave Theory Tech.*, vol. MTT-20, no. 10, Oct. 1972.
- [10] B. Bianco, A. Corana, L. Gogioso, and S. Ridella, "Open-circuited coaxial lines as standards for microwave measurements," *Electron. Lett.*, vol. 16, no. 10, May 1980.
- [11] J. Dibeneditto and A. Uhler, Jr., "Frequency dependence of 50- $\Omega$  coaxial open-circuit reflection standard," *IEEE Trans. Instrum. Meas.*, vol. IM-30, no. 3, Sept. 1981.
- [12] *Hewlett Packard Operating and Service Manual* for HP85050A 7 mm Calibration Kit, Nov. 1986.
- [13] Private communication with Hewlett Packard.

## On the Interaction of the MMIC and Its Packaging

Y. L. Chow, G. E. Howard, and M. G. Stubbs

**Abstract**—The software WATMIC-EMsim [1] is used to simulate the interaction of an MMIC circuit and its packaging. Specifically in this paper, the circuit is the spiral transformer, and the packaging is the surrounding ground ring used to interface the transformer to its coplanar probes. It is found that the resonant frequencies of the transformer are affected greatly with the introduction of the ring but, with its introduction, only slightly by the width of the ring. This paper points out that this finding of interaction mimics the well known phenomenon in electrostatic capacitance. More importantly, this paper points out that in the field theoretic analysis of an MIC/MMIC circuit the influence of the packaging must be considered.

### I. INTRODUCTION

It is pointed out by Montgomery [2] that "(MIC) packages in many applications, will remain both a performance and a cost challenge. Yet, current solid state microwave R & D is focused almost entirely on chips, with little attention to package concerns."

As a small first step in the direction of packaging, this paper studies the interaction between a monolithic microwave integrated circuit (MMIC) spiral transformer and its surrounding ground ring as shown in Fig. 1. As recognized there the ring is used as a ground and as an interface between the transformer and the measuring coplanar probes.

The interaction is studied for the same transformer but with a ring of different widths. One special case of interest is that having the width reduced to zero, i.e., the ring is deleted. It is found that there is a great effect in the resonant frequencies of the transformer

Manuscript received May 18, 1989; revised January 13, 1992.

The authors are with the Faculty of Engineering, Department of Electrical Engineering, University of Waterloo, Waterloo, ON, N2L 3G1, Canada.

IEEE Log Number 9200861.

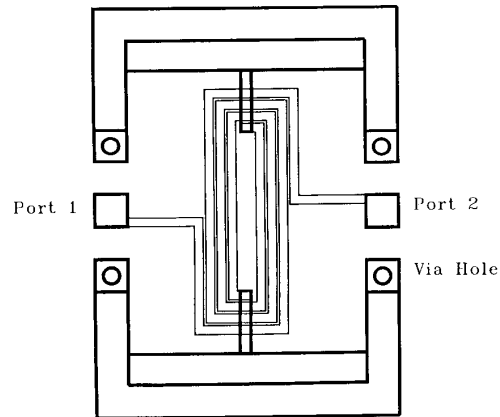


Fig. 1. A spiral transformer with ground ring. The outside dimensions of the ground ring are  $1020 \mu\text{m} \times 710 \mu\text{m}$ . Metallization  $t = 1 \mu\text{m}$  Gold, substrate  $h = 250 \mu\text{m}$ ,  $\epsilon_r = 12.9$ . Dielectric bridge height =  $1.3 \mu\text{m}$ , bridge overlay  $\epsilon_r = 6.8$ . The width of the spiral metallization is  $20 \mu\text{m}$  and the transformer gap is  $6 \mu\text{m}$ .

without and with the ring. However, with the presence of the ring, there is only a small effect with the width of the ring.

Experimentally for MMIC's, changing the ring width is time consuming and expensive. Numerically, on the other hand, electromagnetic simulators such as the software package WATMIC-EMsim [1], the changes can easily be carried out through minor adjustments of the input data. The findings as mentioned in the last paragraph, should be true as numerical technique used has been shown to be quite accurate especially for the MMIC type of MIC circuits [3]-[6].

Despite the above implied accuracy, for a new MMIC structure it is always desirable to have experimental verification and a physical interpretation of the responses of such structures. For the former an experiment on the transformer with a full ground ring, as shown in Fig. 1, is performed and compared with a full numerical simulation. This is given in the next section. For the latter, a numerical experiment on the capacitance to infinity of a metallic box is performed. This is given in Section IV, after the spiral rectangular transformer computations for better interpretation.

### II. AN EXPERIMENTAL VERIFICATION

The transformer with a full ground ring in Fig. 1 is constructed on a GaAs substrate and measured through coplanar probes. The detail of the construction is given in the caption of Fig. 1. Fig. 2 gives the experimental and the computed results of  $S_{11}$  and  $S_{21}$ . We see very good agreement of the results.

With the experimental verification for the full ground ring case we may proceed with confidence to study the computed results from ground rings of various widths, full, half, and zero width, in the next section.

### III. THE WATMIC-EMsim COMPUTATIONS AND GRAPHS

Figs. 1, 3, and 4 show the spiral transformer with three different ground rings. Fig. 4 has the width of the ground ring reduced to zero, i.e., Fig. 4 has no ground ring.

The moment method software WATMIC-EMsim, version 2, is